Materials Science & Engineering A 950 (2026) 149500

Contents lists available at ScienceDirect

Materials Science & Engineering A

journal homepage: www.elsevier.com/locate/msea

Unforeseen precipitation sequences in ex-situ/in-situ TiB_2-reinforced Al2618 Composites Manufactured by Laser-based powder bed fusion

Giorgia Lupi [a], Luca Mariotti [a], Shenglu Lu [b], Wei Xu [c], Luca Patriarca [a], Riccardo Casati [a,*]

[a] Department of Mechanical Engineering, Politecnico di Milano, Via G. La Masa 34, 20156, Milano (MI), Italy
[b] Centre for Additive Manufacturing, School of Engineering, RMIT University, Melbourne, VIC, 3000, Australia
[c] School of Engineering, Deakin University, Victoria, 3216, Australia

ARTICLE INFO

Keywords:
Additive manufacturing
Laser powder bed fusion
Metal matrix composites
Aluminium alloys
Powder functionalization

ABSTRACT

This study explores an innovative hybrid approach for the fabrication of metal matrix composite powder feedstock consisting of Al2618 alloy reinforced with TiB_2. The approach combines pre-alloyed Al2618 powder containing Ti and B to form in-situ TiB_2 with high-energy mechanical mixing to disperse ex-situ TiB_2 on particle surfaces. The feedstock was processed via powder bed fusion - laser beam of metals and subjected to T5 and T6 heat treatments. Microstructural investigations revealed deviations from the typical precipitation and dissolution sequences of conventional Al2618 alloys, attributed to the excess Ti in the pre-alloyed powder, which largely influence the mechanical and physical properties of the material. T5 promoted Al_3Ti and S/S′ precipitates near cell boundaries, leading to UTS and YS of 459 and 433 MPa. T6 produced Ti–Si–rich needle-like phases and Al–Mg–Ti particles that suppressed S′ precipitation. T6 showed the lowest thermal expansion and highest thermal conductivity, attributed to coarser Al_9FeNi precipitates and dissolution of the cellular microstructure. The elastic modulus reached 84.7 GPa (T5) and 82.2 GPa (T6), about 13 % higher than standard Al2618.

1. Introduction

Additive Manufacturing (AM) has continuously expanded over the past years due to its advantages over subtractive manufacturing, such as flexibility, the ability to design complex shapes, and a low buy to fly ratio [1,2]. Among the various AM techniques, the most widely adopted process for metal components is powder bed fusion - laser beam (PBF-LB/M). This process allows for the near-net fabrication of lightweight parts with near-full density and mechanical properties that are comparable to those of conventionally manufactured materials [3–6].

Aluminium alloys are of particular interest for aerospace and automotive applications, where lightweight structures with high specific properties are required. These properties can be further enhanced by adding ceramic or intermetallic particles, producing Al-based metal matrix composites (MMCs) with improved stiffness, strength, wear resistance, and tunable functional behaviour [7,8]. Conventional MMC fabrication routes, however, often suffer from particle segregation and poor machinability, whereas AM can offer a viable solution to overcome these challenges, being able to produce near net shape parts and use evenly reinforced metal powder as feedstock material [9].

A major challenge in PBF-LB/M of high-strength Al alloys is their susceptibility to hot cracking [10–15]. One approach to address these challenges is modifying the chemical composition of the powders by introducing specific alloying elements, such as Zr, Sc, Ti, and B [16–20]. In particular, the combined addition of Ti and B promotes in-situ TiB_2 formation, refining grains and reducing hot-crack sensitivity [21–24]. For example, in a recent study, Belelli et al. modified a 2xx alloy with 2.7 wt% Ti and 0.8 wt% B, promoting the formation of TiB_2 in the molten metal. The pre-alloyed powder exhibited superior PBF-LB/M processability compared to the unmodified alloy, resulting in a fine equiaxed microstructure free from cracks [25]. After heat treatment, the manufactured specimens displayed a yield strength (YS) of 495 MPa and an ultimate tensile strength (UTS) of 460 MPa, as well as excellent mechanical stability at elevated temperatures [26]. Previous works also assessed the effect of alloying with an excess in Ti in TiB_2 reinforced Al alloys, which leads to the formation of a thin Al_3Ti layer at the surface of TiB_2 particles. The nucleation of α-Al requires less undercooling in the presence of Al_3Ti compared to TiB_2, indicating that Al_3Ti acts as a more effective nucleant [22,27–29].

Ex-situ TiB_2 additions have similarly been shown to refine grains and improve processability [30–32]. Several techniques are available to functionalize the surface of the powder particles [33–35]. Mechanical

* Corresponding author.
E-mail address: riccardo.casati@polimi.it (R. Casati).

https://doi.org/10.1016/j.msea.2025.149500
Received 19 September 2025; Received in revised form 19 November 2025; Accepted 20 November 2025
Available online 21 November 2025

mixing or low-energy ball milling has been shown to promote a homogeneous distribution of the reinforcement phase while preserving the spherical powder morphology required for PBF-LB/M process [36–40]. Nevertheless, a previous work by some of the authors of this paper demonstrated that pre-alloying with Ti and B is more effective for grain refinement than ex-situ additions alone [41].

However, producing Al powder feedstock with high amounts of Ti and B via gas atomization remains challenging. B reacts with Ti in the molten Al to form TiB_2 that tends to separate from the liquid phase, causing non-homogeneous boride distribution and leading nozzle clogging during powder production [42–44]. In addition, Ti and B may alter precipitation behaviour during heat treatment [45]. To the authors' knowledge, no work investigated the precipitation behaviour of Ti and B-modified 2xx alloys. Understanding their effects is essential for the development of new alloys with tailored mechanical and physical properties.

In this work, a hybrid approach has been developed to produce an in-situ/ex-situ TiB_2-reinforced Al2618 composite powder. This includes the combination of grain refinement given by the in-situ addition of Ti and B in gas atomized powder and the possibility to reach higher percentage of TiB_2 by the ex-situ method. The gas atomized Al2618-2.1Ti-0.7B (wt.%) powder was high-energy mixed with additional 4.7 wt% of TiB_2 particles to target a total amount of reinforcing particles of 7 wt%, with the aim to enhance the material's elastic modulus and mechanical strength of the Al alloy. Such composite powder was successively processed by PBF-LB/M to produce bulk samples. The printed material was heat-treated according to different schedules to investigate their effect on the microstructure of the MMC material. Particular attention was given to the precipitation sequences in directly aged samples and solution treated and aged materials by means of transmission electron microscopy (TEM) and thermodynamic simulations. The samples were then tested to assess their tensile properties and physical properties, including coefficient of thermal expansion and thermal conductivity. This study provides new insights into the design of MMCs for AM, demonstrating that a combination of in-situ and ex-situ reinforcements, along with appropriate heat treatments, can significantly enhance the performance of high-strength Al alloys. Extensive microstructural analyses were carried out to correlate the observed mechanical and physical properties with microstructural features and precipitation phenomena.

2. Materials and methods

2.1. Powder feedstock

Al2618 powder pre-alloyed with Ti and B was produced by Kymera International [46] through gas atomization. The chemical composition is reported in Table 1. Al powder has D10, D50, and D90 values of 28.6 μm, 43.3 μm and 66.0 μm, respectively. The total amount of in-situ TiB_2 particles is 2.3 wt%. Subsequently, the pre-alloyed powder particles were mixed with TiB_2 particles (4.7 wt%). This step was performed by IMR Metal Powder Technologies Gmbh [47] using a high-energy dry mixer. The process was conducted under nitrogen at room temperature, with the mixer equipped with an internal cooling system to reduce the heat generated by particle friction. TiB_2 particles, with average diameter of 2 μm, were supplied by Treibacher industrie AG [48].

2.2. PBF-LB and heat treatments

A commercial dual-laser PBF-LB/M printer (SLM280, SLM Solutions) was used to manufacture the samples for microstructural characterization and for the evaluation of the physical and mechanical properties of the bulk material.

Three print jobs were performed to assess the printability of the composite powder and to optimize the printing parameters to achieve samples with maximum density. The main parameters that were iterated included laser power, hatch distance, scan speed, and layer thickness. The relative density of samples was evaluated on polished cross sections parallel to the building direction using ImageJ software. Optical microscopy was performed with a Nikon Eclipse LV150NL light optical microscope (LOM) with a 25 × objective lens. The set of parameters that allowed achieving the highest material density (99.6 %) is reported in Table 2. Table 3 summarizes the type and number of printed specimens use for the tests. Further details on each specimen are provided in the following sections.

Different heat treatment schedules were investigated. The T6 heat treatment cycle consists of solution treatment, quenching, and artificial aging. The samples were first solution treated at 530 °C for 1 h, followed by water quenching (WQ). The specimens were then subjected to artificial aging at 180 °C for different durations (0.5, 1, 2, 4, 8, and 24 h). The second thermal treatment schedule consisted of a direct aging process at 180 °C (T5) which was investigated using the same aging times. To evaluate the effect of these heat treatments, Vickers microhardness measurements were performed using a Future-Tech FM-810 system, applying a 300 g_f load with a dwell time of 10 s. The results were reported in terms of hardening curves, considering average values and standard deviations.

2.3. Microstructural characterization

The analysis of microstructures of bulk samples at relatively low magnification was performed by LOM and a field emission scanning electron microscope (SEM, Zeiss Sigma 500) equipped with energy dispersive X-ray analysis (EDX) and secondary electron and backscattered electron detectors (EBSD). Chemical etching with Keller's reagent was performed to reveal the microstructural features.

Scanning transmission electron microscopy (STEM) and high-resolution transmission electron microscopy (HRTEM) analyses were carried out on as-built (AB), solution-treated (ST), T6, and T5 samples.

STEM analysis was performed using a TALOS F200X G2 microscope (Thermo Fisher Scientific), equipped with a high-brightness X-FEG field emission gun (80–200 keV) and four in-column SDD Super-X detectors for energy-dispersive X-ray spectroscopy (EDS). High-angle annular dark field (HAADF), bright-field STEM (BF-STEM) imaging, and EDS mapping were employed to investigate the nanoscale elemental distribution. HRTEM analysis was conducted using a JEM 2100 microscope (JEOL, Japan), also equipped with a field emission gun (FEG, 80–200 keV) and an Oxford X-MaxN 80T EDS detector.

Additionally, Fast Fourier Transform (FFT) analysis was applied to high-resolution STEM and HRTEM images to examine the crystallographic structure of the phases. Post-processing, including FFT analysis, was performed using Digital Micrograph software. For both STEM and HRTEM analyses, foils were extracted parallel to the build direction using a Precision Ion Polishing System (PIPS).

2.4. Mechanical testing

Tensile tests were performed on tensile specimens with a geometry

Table 1
Nominal chemical composition of the pre-alloyed Al2618 powder (wt%).

Cu	Fe	Mg	Ni	Si	Ti	Zn	B	Al
2.4	1.3	1.7	1.2	0.2	2.1	0.01	0.7	Balance

Table 2
Optimal combination of process parameters.

Layer thickness [mm]	0.03
Platform temperature [°C]	70
Laser power [W]	325
Hatch distance [mm]	0.11
Scanning speed [mm/s]	1100
Volumetric energy density [J/mm^3]	53.7

Table 3
Blank geometries, printing orientations, and quantities of the specimens used in this work.

Test type	Dimensions [mm]	Number
Metallography	10 × 10 x 10	12
Tensile tests	D14 x L110	6
CTE	D8 x L50	3
LFA	D13 x L30	3

reported in Fig. S1 of the Supplementary Material 1. To assess the effect of the different heat treatment routes, the specimens were tested both in T6 and T5 conditions. Tensile tests were performed using an MTS-Alliance RT/100 universal testing machine. Vickers microhardness measurements were performed using a Future-Tech FM-810 system, under a 300 g_f load with a dwell time of 10 s.

For the evaluation of the elastic modulus, the testing procedure consisted in repeating 10 quasi-static loading cycles between 10 % and 40 % of yield stress. The final elastic modulus values are the average of the repeated cycles (excluding the first two which are affected by machine alignment and plays).

2.5. Physical properties

The coefficient of thermal expansion (CTE) was measured on samples with a diameter of 8 mm and a height of 10 mm. Tests were conducted on specimens in AB, T6, and T5 conditions using a Vertical Dilatometer Linseis V75 in a vacuum atmosphere. The temperature was increased at a rate of 2 °C/min up to 300 °C. Two repetitions for each condition were performed.

The thermal diffusivity of the material in AB, T5, and T6 conditions was measured using the Linseis LFA 1000/1600 Laser Flash Analyzer (LFA). The tests were conducted in a vacuum atmosphere within a temperature range of 20 °C–300 °C. The LFA samples had a diameter of 13 mm and a height of 3 mm. Both faces of the specimens were polished using a 1 μm diamond suspension, and a thin graphite layer was sprayed on both surfaces to enhance laser energy absorption. To evaluate the thermal conductivity of the samples, the specific heat capacity (C_p) and density were estimated within the same temperature range using the Thermo-Calc software [49] with the TCAl8 database.

3. Results

3.1. Powder characterization

Fig. 1a shows the cross-section of a pre-alloyed powder particle, where fine TiB_2 particles (<1 μm) formed in situ are distributed within the Al matrix. In this study, the highest Ti and B concentrations obtained were 2.1 wt% and 0.7 wt%, respectively, corresponding to a total TiB_2 content of 2.3 wt% considering the excess of Ti.

The pre-alloyed Al2618 powder was further mixed with TiB_2 particles via HEM. This ex-situ process enables the attachment of additional TiB_2 particles onto the surface of pre-alloyed powder particles (Fig. 1b). As a result, the TiB_2 particles appear well dispersed and uniformly distributed. Moreover, the functionalized powder particles largely maintain their original spherical morphology, which is crucial for ensuring good flowability and processability in the subsequent AM step. This approach has proven to be effective in reaching a total TiB_2 content of 7 wt% (4.5 vol%).

The impact energy applied during HEM is sufficient to promote strong interfacial interactions, improving the adhesion of TiB_2 particles to the metal powder. Moreover, in our recent work [41], MMC powders functionalized with ex-situ TiB_2 particles by HEM were sieved after the powder functionalization process to provide valuable insights into the reusability of the powders. The results showed that the sieving process does not significantly impact the powder configuration, and particularly the amount of reinforcements attached to the powder surface for the HEM powder feedstock. Consequently, these powders can be reused in successive PBF-LB/M printing without the need for reprocessing to enhance homogeneity.

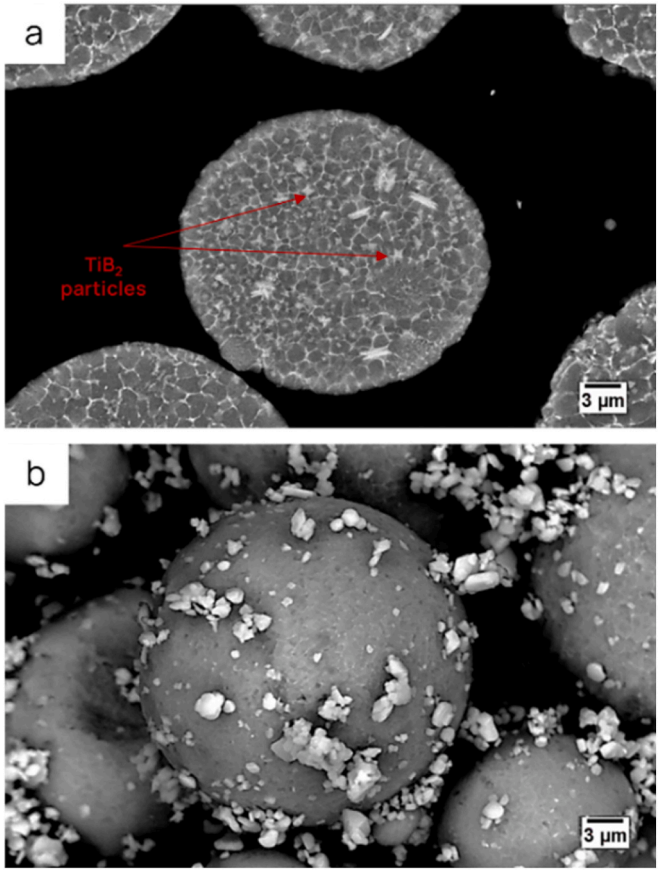

Fig. 1. SEM micrographs of the powder feedstock. a) cross-section of the pre-alloyed powder where the red arrows indicate TiB_2 particles and b) composite powder feedstock after high-energy mechanical mixing. (For interpretation of the references to colour in this figure legend, the reader is referred to the Web version of this article.)

3.2. Characterization of as-built material

Following the optimization of process parameters, bulk samples were successfully printed and characterized to evaluate their microstructures and mechanical properties. The density analysis of bulk samples was conducted by examining the cross sections, both normal and parallel to the z-axis, of three cubes following the ASTM F3637−23 standard [50]. Image analysis was performed with ImageJ to evaluate the relative density of the samples, which was found to be 99.6 ± 0.1 %.

SEM analysis of the as-built sample provided insight into the shape, size, and distribution of TiB_2 particles within the bulk material. The micrographs in Fig. 2a and b reveal a homogeneous dispersion of the reinforcement phase, without visible solidification cracks. Moreover, Fig. 2b shows the typical PBF-LB/M cellular structure with equiaxed α-Al cells surrounded by a continuous segregation network.

Regarding the in-situ formed TiB_2 particles, it was possible to detect their presence by STEM analysis, as shown in Fig. 2c.

In addition, STEM analysis confirmed the presence of a thin layer enriched in Al and Ti surrounding the in-situ formed TiB_2 nanoparticles. By combining FFT analysis and STEM-EDS data (see Fig. S2 of Supplementary Material 1), this layer can be identified as an Al_3Ti crystalline phase. Moreover, near the TiB_2 nanoparticles, spherical Cu-bearing particles were also identified. FFT analysis of STEM images reveals the

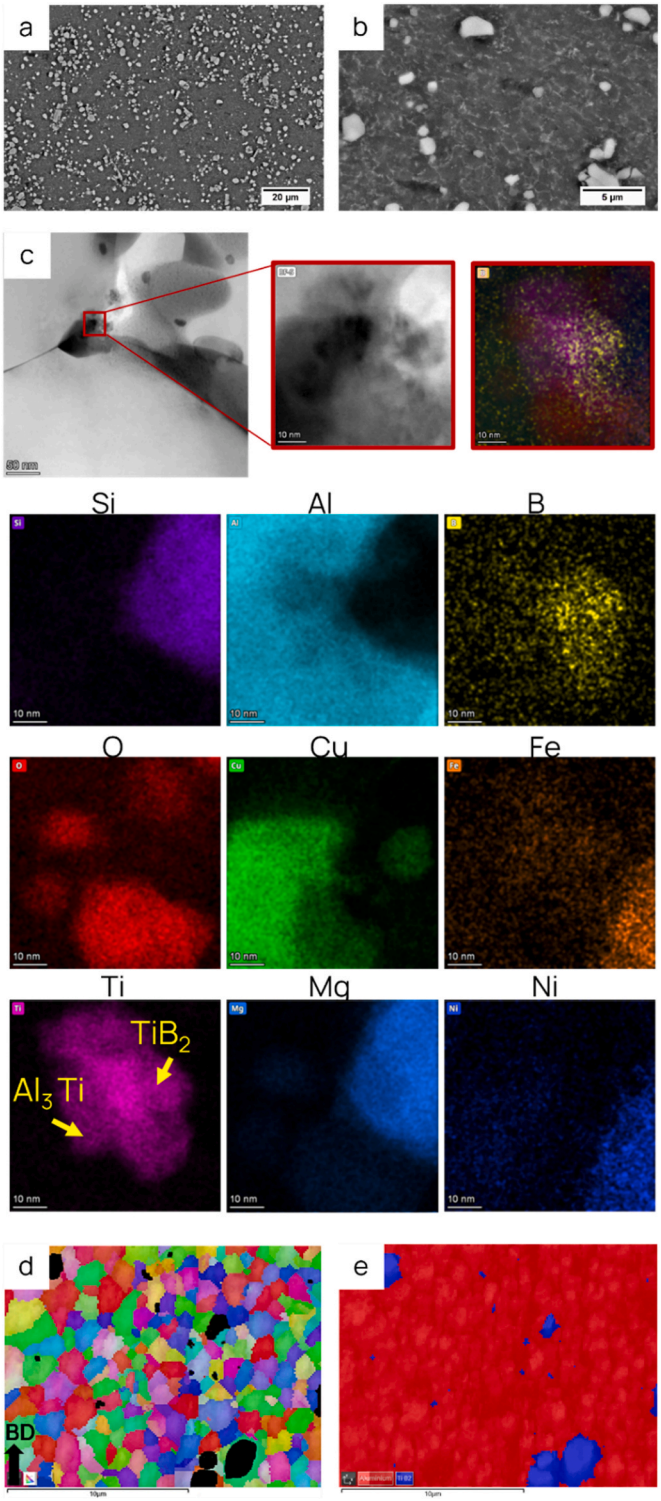

Fig. 2. a), b) SEM micrographs of the cross-section parallel to the building direction of the material in AB condition. The light grey particles correspond to the ex-situ TiB_2 particles. c) STEM-BF-S micrograph, STEM-EDS of the highlighted area and overlap of different EDS elemental maps of the material in the AB condition. EBSD results: d) IPFz map, and e) phase map. In the IPFz map, TiB_2 grains were excluded from the analysis and are represented in black. In the phase maps the Al matrix is red, and TiB_2 particles are blue. (For interpretation of the references to colour in this figure legend, the reader is referred to the Web version of this article.)

formation of Al_2CuMg precipitates (see Fig. S2 of Supplementary Material 1).

EBSD analysis was performed to evaluate the efficacy of borides in suppressing epitaxial growth of columnar grains from previously deposited layers (Fig. 2d and e). The result is a fine equiaxed microstructure with no visible cracks. The grains have an average area of 0.73

μm^2 and an average diameter of 0.87 μm.

3.3. Precipitation behaviour and microhardness evolution during heat treatment

Aging curves based on microhardness vs. time have been collected in Fig. 3a to select the treatment parameters to reach the peak-aged condition starting from the as-built and solution treated samples. The hardness of the as-built material is 152 ± 2 H V (corresponding to the 0 h point of the black curve), indicating that the presence of in-situ and ex-situ borides effectively increases the material's hardness compared to that of 104 H V for an unreinforced Al2618 alloy produced by PBF-LB/M in the same condition [51]. After solution treatment at 530 °C followed by WQ (0 h point of the red curve), the hardness drops to 113 ± 2 H V. The solution treated sample reaches a hardness-peak value of 149 ± 4 H V after 1 h of aging at 180 °C (T6 condition). In contrast, the peak hardness for the T5 condition (154 ± 2 H V) is reached" after 2 h at 180 °C. The initial decrease in hardness observed for the T5 condition (from 152 H V to 140 H V after 1 h) can be attributed to stress relaxation induced by the heat treatment, which reduces internal residual stresses generated during the printing process. For the sake of comparison with T5, an aging time of 2 h was selected for T6 samples instead of 1 h, as the hardness values of the samples aged for 1 h (149 ± 4 H V) and 2 h (147 ± 4 H V) are very similar.

The microstructure of the heat-treated samples is shown in Fig. 3. In both cases, ex-situ coarse TiB_2 particles are visible in the Al matrix; these particles are not affected by the different heat treatments since their size, shape and distribution resemble that of the material in as-built condition. The T5 sample preserves the cellular structure that is typical of the AB condition (Fig. 3b), with higher concentrations of Cu, Fe, and Ni at the cell boundaries [51].

In contrast, the microstructure of the T6 sample undergoes significant changes (Fig. 3c), characterized by the disappearance of the typical cellular structure observed in the AB and T5 samples, and the emergence of coarser secondary phases. EDS chemical analysis revealed that these secondary phases are enriched in Fe and Ni, suggesting that they can be identified as Al_9FeNi phase, a typical phase found in Al2618 alloy produced by AM, as well as conventional methods [25].

A more in-depth investigation was carried out using STEM and HRTEM to gain insight into the type, size, and distribution of sub-micron and nano-sized precipitates. The material was analysed in ST, T6 (ST+180 °C, 2 h) and T5 (180 °C, 2 h) conditions. Representative STEM images are presented in Fig. 4.

Fig. 4a illustrates the microstructure of the alloy after solution treatment. Most of the Cu-bearing particles found in the AB alloy dissolve into the Al matrix, indicating that Cu is retained in solid solution. The presence of particles rich in Ni and Fe suggests that Al_9FeNi phases remain stable even after solution treatment. This is consistent with previous literature results, where these phases have been reported to remain stable during heat-treatment and to play a significant role in enhancing mechanical strength and microstructural stability at elevated temperatures [25,52]. Ti–Si-rich precipitates forming needle structures arranged in a corona-like pattern were also detected (Fig. 4b). The precipitation of such phases is uncommon in conventionally processed Al2618 alloys, where Si usually remains in solid solution or forms Mg–Si-based precipitates [53]. Three TiAlSi compounds have been reported as potentially stable in Si- and Ti-bearing Al alloys: $(Al,Si)_3Ti$, τ_1 $Ti_7Al_5Si_{12}$, and τ_2 $(Al,Si)_2Ti$. The τ_2 compounds can be considered $TiSi_2$-based phases, where Ti and Si atoms are partially replaced by Al. These phases often show a lamellar structure, appearing as a mixture of $(Al,Si)_3Ti$ and τ_2 [54,55]. Ma et al. demonstrated that this mixture results from a eutectoid transformation $(Al,Si)_3Ti \rightarrow \tau_2 + Al$, occurring during solution heat treatment [56]. Wang et al. reported that the formation of Al–Si–Ti phases is likely to suppress the precipitation of β'' and β′ Mg_2Si precursors, modifying the overall aging behaviour of the alloy. They also found that blocky-shaped $(Al,Si)_3Ti$ particles with an average size of 5–6 μm were formed, which increased strength but decreased ductility [57]. HRTEM analyses, combined with FFT and selected area electron diffraction (SAED) patterns (Fig. 2b), revealed that the crystal structure of these Ti–Si-rich precipitates resembles that of orthorhombic Al_3Ti (see Fig. S3 of Supplementary Material 1). The measured *d*-spacings from the FFT and SAED patterns are consistent with those of the Al_3Ti phase, although slight deviations were observed. These discrepancies can be attributed to the partial substitution of Al atoms by Si in the $(Al,Si)_3Ti$ structure, which alters the lattice parameters compared to stoichiometric Al_3Ti. This structural similarity supports the identification of the observed precipitates as $(Al,Si)_3Ti$. Additionally, Mg is primarily associated with O, presumably due to the formation of a $MgAl_2O_4$ spinel. In the AB condition, Mg is mostly found in combination with Si at cell boundaries, likely forming Mg_2Si. After solution treatment, most of the Mg is dissolved in the α-Al matrix, with only small Mg-rich particles detected, primarily associated with oxygen and occasionally found near Ti-Si-rich precipitates.

After aging treatment (T6), the Ti–Si-rich precipitates forming needle structures in a corona pattern remain present, indicating their high stability after exposure at 180 °C (Fig. 4c). Al_9FeNi precipitates are still present (see Fig. S4 of Supplementary Material 1). However, typical S and S′ phases, commonly observed as needle precipitates in conventional Al2618 alloys [51,58], were not found in the aluminium matrix. Mg is found associated with O, likely forming spinel phases such as $MgAl_2O_4$,

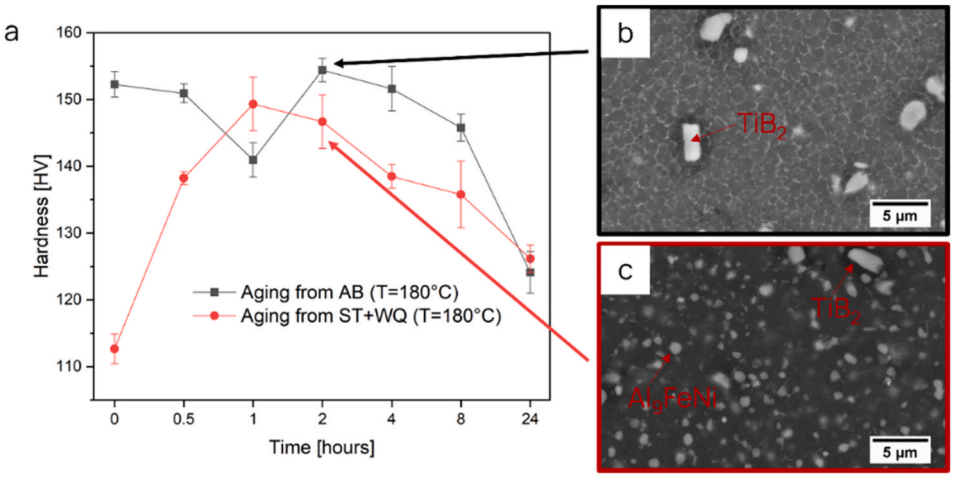

Fig. 3. a) Age-hardening curves obtained by exposing ST + WQ and AB materials to 180 °C for varying durations. SEM micrographs of the composite in b) T5 and c) T6 temper conditions.

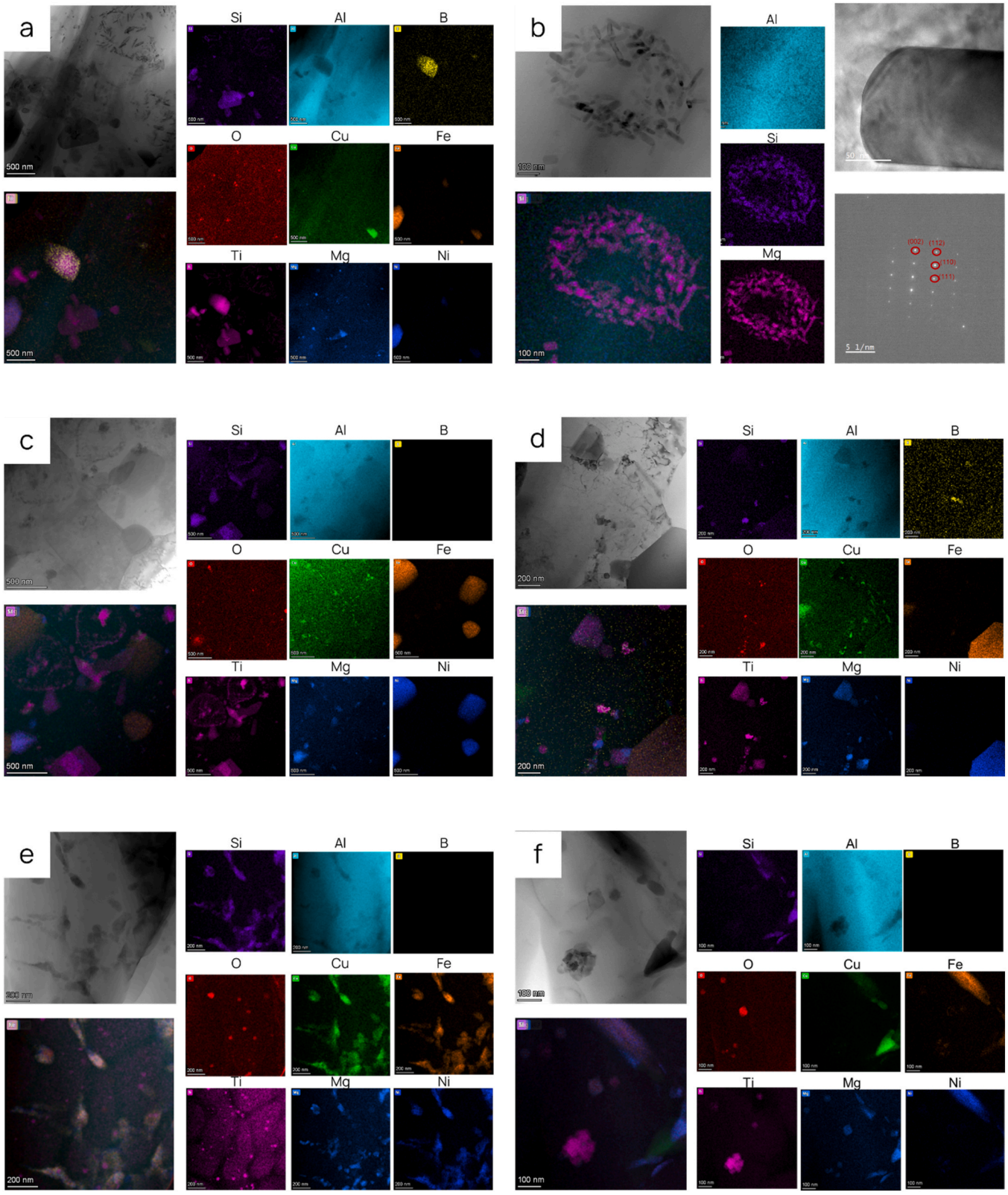

Fig. 4. STEM-BF-S image, STEM-EDS and overlap of different EDS elemental maps of the material in a), b) ST, c), d) T6, and e), f) T5 conditions. In b) HRTEM image SAED pattern of $(Al,Si)_3Ti$ precipitates are included.

as well as with Si, where Mg_2Si precipitates form. Mg is also found to be bound with Ti, resulting in the formation of Ti–Mg containing precipitates (Fig. 4d).

The last analysed condition, direct aging (T5), reveals that the material retains the cellular structure observed in the AB condition, with micro-segregations along the cell boundaries (Fig. 4e and f). These regions are enriched in Mg, Si, Cu, Fe and Ni, leading to the formation of Mg_2Si and Fe,Ni- and Cu, Ni-bearing phases. FFT analysis confirms the

presence of Al_9FeNi and Al_7Cu_4Ni (see Figure S5 and Figure S6 of Supplementary Material 1), in agreement with previous literature results [59]. Additionally, nanoscale Ti-rich precipitates are detected within the matrix, which correspond to Al_3Ti as suggested by FFT analysis (see Fig. S7 of Supplementary Material 1).

HRTEM imaging performed along the $[001]_{Al}$ zone axis (Fig. 5a) in T5 condition reveals the presence of additional nanoscale precipitates located predominantly in the regions close to the cell boundaries. These precipitates appear as lath-shaped features aligned along $<100>_{Al}$ directions. The black dots are the extremities of S/S′ precipitates lying perpendicular to the $(001)_{Al}$ plane. The morphology and orientation are consistent with S/S′ precipitates, as supported by the SAED analysis (inset in Fig. 5a), where extra diffraction spots are observed in addition to the fundamental Al reflections [60,61]. These additional diffraction spots are very similar to the S/S′ reflections and double diffraction patterns proposed by Wang et al. [62]. Precipitation of S/S′ (Al_2CuMg) is favoured at the cell boundaries due to higher concentration of Cu and Mg in these regions, likely resulting from rapid solidification that limits solute redistribution within the grains. To validate this hypothesis, S/S′ precipitation kinetics were simulated using the Thermo-Calc PRISMA module, considering two distinct compositional regions: a solute-rich cell boundary and a solute-depleted cell core. To define appropriate chemical compositions for these regions, a Scheil-Gulliver solidification simulation was performed for the Al2618 alloy. During solidification, the cell core forms first (at the liquidus temperature) and then grows radially outward toward the cell boundaries [63]. Accordingly, in Fig. 5b, a mass fraction of solid equal to 0.0 corresponds to the cell core, while 1.0 corresponds to the cell boundary. The TC-PRISMA module was then employed to simulate the precipitation of S and S′ phases in both regions (Fig. 5c and d). Under the applied thermal profile, the boundary composition leads to a higher total volume fraction and growth of S and S′ phases after 2 h at 180 °C, with a mean precipitate size of about 9 nm. Moreover, the S phase appears to be the most likely to form at the cell boundary. In contrast, the core composition results in a much lower volume fraction and smaller precipitate size (<1 nm), confirming that precipitation is substantially suppressed due to the limited availability of Cu and Mg at the cell core.

3.4. Mechanical properties

Tensile tests were carried out at room temperature on T5 and T6 specimens. Representative tensile curves are shown in Fig. 6. Yield strength (YS), ultimate tensile strength (UTS), elastic modulus (E), and elongation at fracture values are reported in Fig. 6. The alloy in T5 condition revealed the highest UTS and YS, showing the capability of the alloy to respond to direct aging. The elastic modulus of the composite alloy reached values of 82.2 GPa and 84.7 GPa in the T6 and T5 conditions, respectively.

The tensile stress-strain curves of the tested specimens exhibit serrated yielding, a characteristic feature of the Portevin–Le Chatelier (PLC) effect, as indicated by the fluctuations in the flow stress. The PLC effect is a phenomenon associated with dynamic strain aging (DSA), which occurs due to the interaction between mobile dislocations and diffusing solute atoms. This interaction leads to localized strengthening and sudden stress drops, resulting in an unstable plastic flow [64,65]. Similar behaviour has been observed in high-strength Al–Cu–Mg alloys, where the presence of fine precipitates and solute atoms promotes DSA [66,67]. A distinct upper and lower yield point is more pronounced in the T5 condition. Indeed, the T5 condition retains a high density of residual dislocations and solutes in solid solution. This promotes the

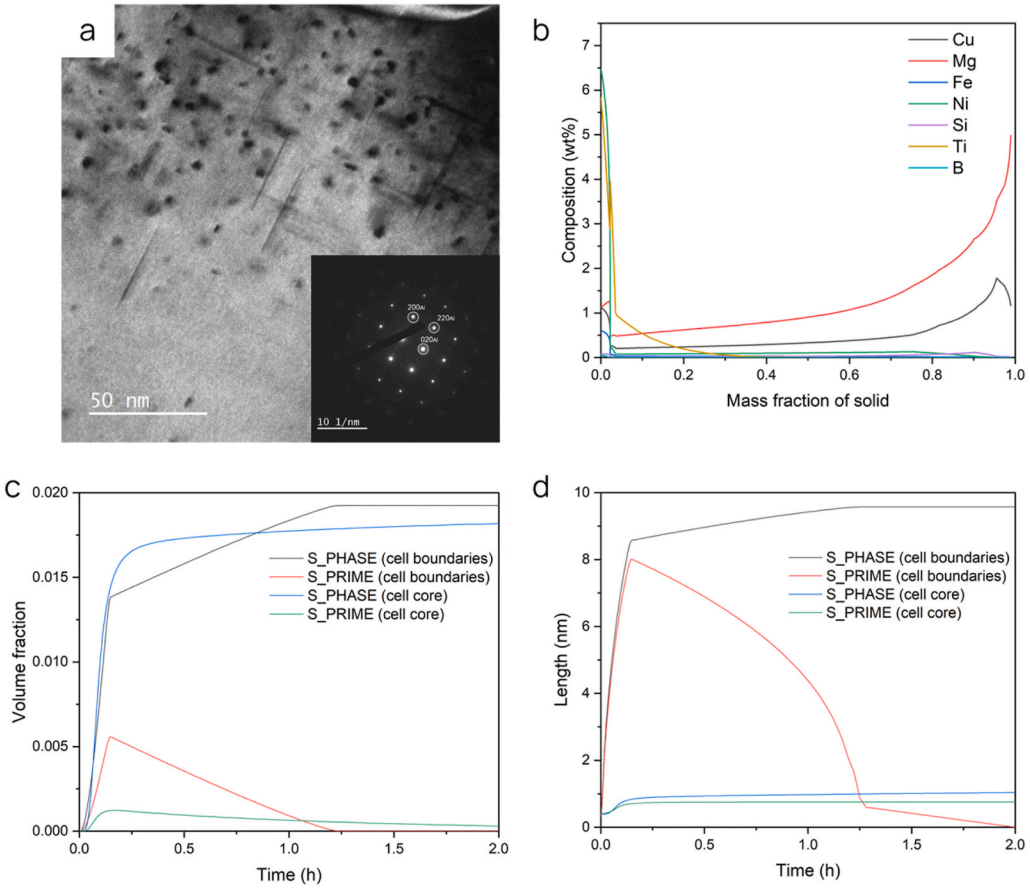

Fig. 5. a) HRTEM image and b) SAED pattern performed along the $[001]_{Al}$ zone axis of the material in T5 condition. b) Scheil-Gulliver solidification curves. c) Volume fraction and d) Length of S and S′ precipitates simulated using Thermo-Calc PRISMA under T5 condition (180 °C, 2 h).

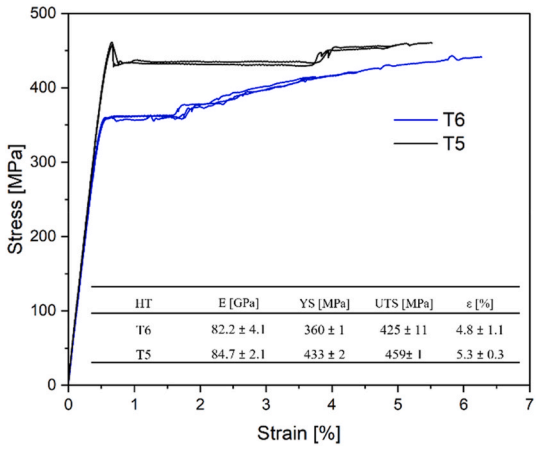

Fig. 6. Representative tensile curves of the T6 and T5 specimens.

dynamic interaction between dislocations and solutes, leading to discontinuous yielding behaviour characterized by a pronounced upper and lower yield point. In contrast, the T6 condition reduces solute content in solid solution and promotes recovery of the dislocation network [68–70].

3.5. Thermo-physical properties

Studying the physical properties of Al2618, such as CTE and thermal conductivity, is crucial given its intended use in high-temperature applications. Ensuring dimensional stability and effective heat dissipation is fundamental to prevent thermal stress and potential failures during service. In particular, the impact of heat treatments on these properties is of interest, as they significantly affect microstructural evolution, precipitate formation, and residual stress states in the alloy.

In MMCs, the matrix-reinforcement interface plays a critical role, as thermal residual stresses generated at the interface impact the CTE. The size and distribution of TiB_2 particles further contribute to the degree of matrix constraint during thermal expansion. Heat treatments can also modify the CTE by affecting the microstructure, phase distribution, and internal stress state of the material [71,72]. To investigate these effects, the CTE was measured in the AB, T5, and T6 conditions, and the results are presented in Fig. 7a.

The material in the AB condition shows the highest CTE (28.4×10^{-6} 1/K), followed by T5 (22.2×10^{-6} 1/K) and T6 (22.5×10^{-6} 1/K) conditions. The differences between T5 and T6 are quite minor, making it challenging to conclude which heat treatment is more effective in reducing the CTE. Several aspects can be considered to explain the influence of heat treatment on CTE such as the release of residual stresses built up during the PBF-LB/M, the formation and coarsening of precipitates, and changes in the elastic modulus [73]. Several studies have reported a higher CTE in different AB materials, often attributed to the presence of residual stresses introduced during the PBF-LB/M process [74–76]. Microstructural factors also play an important role in CTE. Indeed, controlling the grain size and promoting the formation of coherent precipitates within the composite are essential strategies to tailor the CTE [77]. It was observed that T5 heat-treatment leads to a decrease in CTE. In the present case, the reduction of CTE following T5 heat-treatment can be attributed to several factors, including stress relaxation and precipitation of Al_3Ti particles with a lower CTE compared to the Al2618 matrix [78]. The T6 condition shows a reduction in CTE compared to the AB condition, similar to that observed in T5. However, the T6 condition appears more thermally stable, as the CTE values remain consistent across both measurement cycles, suggesting that the microstructure has stabilized. This stability may be related to the formation of larger Al_9FeNi precipitates, further restricting thermal expansion of the composite material. Previous studies have shown that CTE decreases with increasing fraction and size of precipitates. The decrease of CTE is attributed to the formation of precipitates, which creates additional interfaces in the alloy and impedes the thermal expansion of the Al matrix [77,79].

The thermal conductivity of MMCs is influenced by both the presence of ceramic reinforcements and the applied heat treatments. The microstructures associated with various thermal treatments also affect thermal conductivity by modifying the paths for electron migration and phonon contributions [80–82].

Fig. 7b presents the measured thermal conductivity for the materials in AB, T5, and T6 conditions. The AB material exhibits much lower thermal conductivity compared to that of the material in T6 condition. This difference can be explained by the presence of the characteristic cellular microstructure in the AB condition, which can hinder heat transfer. Indeed, the cell boundaries can act as barriers to heat transfer due to the segregation of alloying elements such as Mg, Si, Cu, Fe, and Ni. In the T5 condition, the retention of the cellular structure, combined with the formation of finely and homogeneously distributed Al_3Ti precipitates (which have low thermal conductivity, 10–12 W/mK [83]), leads to a reduction in thermal conductivity. Precipitates generally reduce the thermal conductivity of metallic alloys by impeding the movement of heat carriers, such as free electrons and phonons [84]. The T6 sample exhibits the highest thermal conductivity among the three

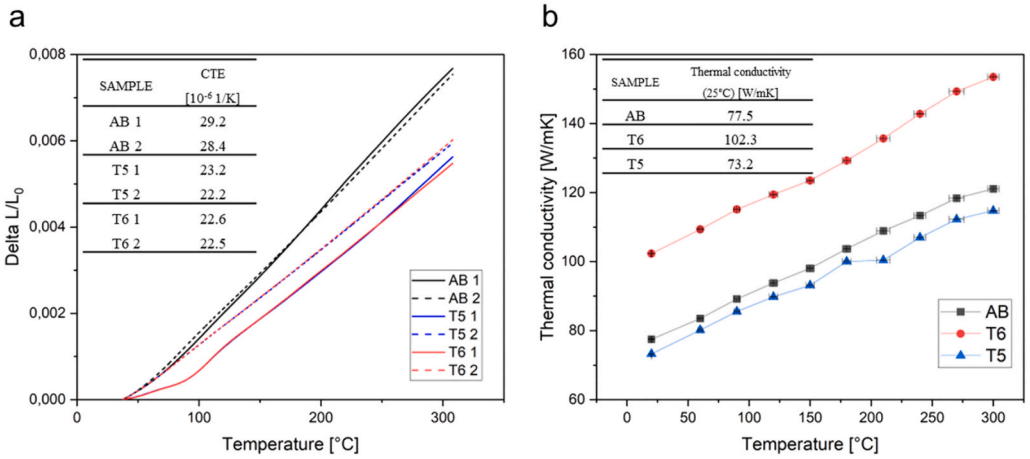

Fig. 7. a) Delta L/Lo curves Vs temperature for the material in different heat-treated conditions. The first test is represented by the solid line, while the curves corresponding to the repeated test on the same sample are shown as dashed lines.
b) Thermal conductivity Vs temperature curves for the material in different heat-treated conditions.

investigated conditions. This improvement is primarily associated with the elimination of the cellular microstructure upon solution treatment and quenching, which results in a more homogeneous microstructure with fewer obstacles to heat transfer. Moreover, it has been reported that the relaxation of residual stresses during solution treatment can contribute to the increase in the thermal conductivity of the material [85]. Finally, thermal diffusivity tends to improve as the solute concentration in the α-Al matrix decreases rapidly [86].

4. Discussion

4.1. Grain refinement in PBF-LB/M Al composites

The powder functionalization method adopted in this work, i.e., pre-alloying by gas atomization followed by HEM, enabled the production of a composite powder feedstock containing 7 wt% (4.5 vol%) TiB_2 reinforcements. The uniform distribution of ex-situ TiB_2 particles observed in the powder (Fig. 1b) confirms the effectiveness of the method in achieving a homogeneous dispersion of reinforcements, both in the powder and consequently in the consolidated composite material. Regarding the in-situ formed TiB_2 particles, it is worth mentioning that their formation occurs during gas atomization, which results in nanometric particles that are beyond the detection capability of SEM, in addition to the micrometric/submicrometric particles pointed out in Fig. 1a. Indeed, it was possible to detect their presence by STEM analysis, as shown in Fig. 2c. In the AB material, TiB_2 nanoparticles are found surrounded by an Al_3Ti layer. As already reported in the literature [25,87], ex-situ and in-situ TiB_2 particles refined the grain structure and reduced the tendency of hot tearing (Fig. 2d and e). TiB_2 particles are grain growth inhibitors in Al alloys, which provide a high density of low-energy barrier nucleation sites ahead of the solidification front. However, while TiB_2 particles contribute to grain refinement by acting as heterogeneous nucleation sites and by pinning grain boundaries, the key factor in achieving the observed fine equiaxed grain structure is the excess Ti present in the pre-alloyed powder [41]. The excess Ti segregates at the surface of TiB_2 particles, leading to the formation of an Al_3Ti crystalline layer. Al_3Ti has been shown to be a more effective nucleant than TiB_2, further enhancing grain refinement [27,28].

4.2. Abnormal precipitation behaviour

Fig. 8 presents a schematic overview of the microstructural evolution observed under various heat-treatment conditions, showing deviation from the typical precipitation sequence of Al2618 alloy. In particular, the excess Ti dissolved in the Al matrix contributes to the precipitation of Ti-rich intermetallics during heat-treatments.

After solution treatment, $(Al,Si)_3Ti$ precipitates forming needle structures arranged in a corona-like pattern were detected (Fig. 4b). After aging treatment (T6), these precipitates remain present, indicating their stability after exposure at 180 °C (Fig. 4c). However, typical S and S′ phases, commonly observed in the form of needle precipitates in conventional Al2618 alloys [51,58], were not found in the aluminium matrix. This absence suggests a deviation from the expected precipitation behaviour under the aging conditions for this alloy. Indeed, in the case of 2xx series alloys with Cu/Mg ratio <1.5 at.%, the widely accepted precipitation sequence is:

SSSS → GPB zone → S″ (GPB2) → S′ → S (Al_2CuMg)

Where SSSS refers to the Supersaturated Solid Solution, GPB to the Guinier–Preston–Bagaryatsky zones, and the S′ precursor of the S phase is known to be the main contributor to peak strengthening [88–90]. Moreover, it has been reported that depending on the alloy composition, particularly the Cu content and the Cu/Mg ratio, and ageing parameters, different phase distributions, and consequently different material characteristics, can be obtained [91].

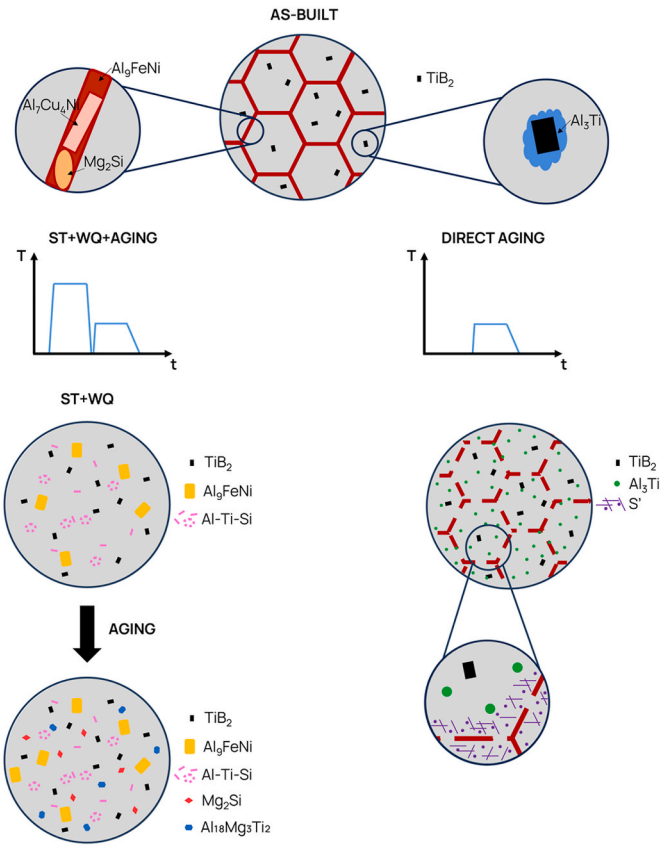

Fig. 8. Schematic of the precipitation behaviour.

Ti–Mg containing precipitates were also detected in the Al2618 matrix after aging (Fig. 4d). This observation aligns with the findings in the literature for Al-Cu-Mg alloys modified with Ti. Kun et al. reported the presence of Al-Mg-Ti precipitates ($Al_{18}Mg_3Ti_2$), that are known to enhance the strength of Al-Cu-Mg-Ti alloys at elevated temperatures. However, similar to the findings of this work, they noted that the formation of $Al_{18}Mg_3Ti_2$ particles inhibits the precipitation of the S/S′ phase [92]. Thus, the lack of S and S′ precipitates observed in the present study may be attributed to the formation of these alternative Ti–Mg--containing phases. This contrasts with the behaviour of conventionally processed Al2618 alloys, which typically exhibit a marked increase in hardness upon aging due to the precipitation of fine S/S′ phases [93]. Lastly, after T6 heat treatment, coarse Al_9FeNi precipitates are found.

The material in T5 maintains the cellular structure observed in the AB condition, with micro-segregations along the cell boundaries (Fig. 4e and f). Al_3Ti nanoprecipitates are also found to be homogenously dispersed in the Al matrix. These precipitates can contribute to precipitation strengthening and thermal stability, enhancing the mechanical properties of the alloy. The T5 heat treatment is also characterized by the formation of S/S′ precipitates primarily at the cell boundaries (Fig. 5a). HRTEM analysis and Thermo-Calc PRISMA simulations reveal that S/S′ (Al_2CuMg) precipitates preferentially form at cell boundaries, where Cu and Mg concentrations are higher.

4.3. Enhancement in strength and stiffness via reinforcement

The different microstructure and precipitates in the T5 and T6 states largely influence the mechanical and thermo-physical properties of the material.

Regarding thermo-physical properties, both heat treatments effectively reduced the CTE compared to the AB condition, with T6 exhibiting greater thermal stability, likely due to the formation of larger Al_9FeNi

precipitates. The T6 condition also showed the highest thermal conductivity, attributed to the homogenization of the microstructure, the elimination of the cellular structure, and the relaxation of residual stresses. In contrast, the T5 condition retained the cellular structure and promoted the formation of finely and homogeneously dispersed Al_3Ti precipitates, resulting in a lower thermal conductivity than the AB condition.

From a mechanical standpoint, the T5 condition provided the highest strength (Fig. 6) due to the retained fine cellular structure and even dispersion of fine Al_3Ti precipitates, which are known to significantly enhance the mechanical properties of the Al matrix at both room and high temperatures [94,95]. In addition, the localized formation of S/S′ precipitates at the cell boundaries provides an additional contribution to strengthening. The T6-treated alloy, characterized by a coarser microstructural feature, displayed slightly higher elongation at fracture but much lower UTS and YS in comparison to the T5 condition.

Comparable elastic modulus values to those obtained in this work were reported by Xi et al. who processed aluminium matrix composites via PBF-LB/M, using pure Al as the matrix and reinforcing it with 10, 15, and 20 wt% (ZrC + TiC) particles. An elastic modulus of approximately 94 GPa and a yield strength of 280 MPa were achieved for the composite containing 15 wt% reinforcement [96]. These comparisons further highlight the promising mechanical performance of the present alloy design, which achieves high stiffness with a considerably lower reinforcement content.

Table 4 presents a comparison of the mechanical properties of the investigated alloy with literature data on various TiB_2-reinforced and 2xx-series alloys produced via PBF-LB/M. To further support this comparison, Fig. 9 reports Ashby maps of YS *vs.* elongation and YS *vs.* UTS. The present alloy, particularly in the T5 condition, shows a superior combination of high strength and moderate ductility. A yield strength of 433 MPa and elongation of 5.3 % was achieved, outperforming several TiB_2-reinforced systems, which generally suffer from more severe ductility losses at comparable strength levels. Furthermore, the mechanical performance observed is comparable to that of Zr-modified Al2618 alloys, well known for their excellent strength–ductility balance [97]. This underlines the effectiveness of the hybrid reinforcement strategy adopted in this work.

Moreover, as expected for MMCs, the material demonstrates higher strength and stiffness compared to conventional Al2618 alloys, even though with reduced ductility. This is typical of MMCs with a high-volume fraction of ceramic reinforcement [98]. A key highlight of this alloy is its significantly enhanced elastic modulus, which reaches 82.2 GPa and 84.7 GPa in the T6 and T5 conditions, respectively. These values are notably higher than the typical 72 GPa reported for conventional Al2618 alloy [99], confirming the effectiveness of the reinforcement strategy. This improvement can be attributed to the presence of TiB_2 particles, which influence the stiffness of the material. The slightly different Young's moduli observed in the T5 and T6 specimens can be attributed to the different phases (size, nature, and volume fraction) within the two microstructures. For instance, Al_3Ti precipitates have a much higher elastic modulus (217 GPa) than the Al matrix, and their presence can lead to the increase in elastic modulus in the T5 condition [100].

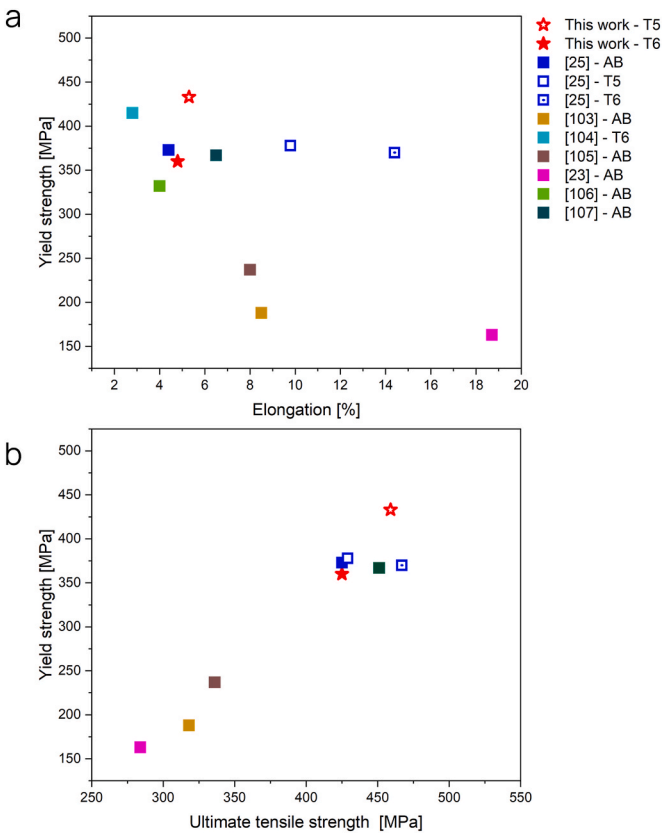

Fig. 9. Ashby maps showing a) YS *vs.* Elongation and b) YS *vs.* UTS for the alloys listed in Table 4.

For comparison, Ma et al. reported significantly lower elastic modulus values of 64.4 GPa and 68.6 GPa for Al2618 alloys reinforced with 4 wt% TiB_2 particles, processed by cold rolling in the as-rolled and T6 states, respectively [101]. In contrast, an A205 alloy with in-situ formed nano-TiB_2 particles produced by PBF-LB/M exhibited a lower elastic modulus of 77.8 GPa [102]. It should be noted that in both cases, the modulus values were derived from the linear elastic part of the tensile stress–strain curves, which may not provide the most accurate measurement of elastic modulus. Comparable elastic modulus values to those obtained in this work were reported by Xi et al. who processed aluminium matrix composites via PBF-LB/M, using pure Al as the matrix and reinforcing it with 10, 15, and 20 wt% (ZrC + TiC) particles. An

Table 4
Comparison of mechanical properties with literature data of various TiB_2-modified and 2xx series alloys, manufactured by PBF-LB/M.

Composition	Heat treatment	Hardness [HV]	UTS [MPa]	YS [MPa]	Elongation [%]	Ref.
Al2618+ ex-situ/in-situ TiB_2	T5	154	459	433	5.3	[This work]
	T6	147	425	360	4.8	
Al2618	AB	104	–	211	–	[51]
	T6	132		316		
Al2618 + Ti/B (pre-alloyed)	AB	117	425	373	4.4	[25]
	T5	128	429	378	9.8	
	T6	142	467	370	14.4	
AlSi10Mg + ex-situ TiB_2	AB	–	318	188	8.5	[103]
AlCuMg + in-situ TiB_2	T6	–	–	415	2.8	[104]
Al2024 + ex-situ TiB_2	AB	–	336	237	8.0	[105]
Al2024 + ex-situ TiB_2	AB	108	284	163	18.7	[23]
Al2618 + Ti/B (pre-alloyed)	AB	120	381	332	4.0	[106]
AlCuMgNi + Ti/B (pre-alloyed)	AB	–	451	367	6.5	[107]

elastic modulus of approximately 94 GPa and a yield strength of 280 MPa were achieved for the composite containing 15 wt% reinforcement [96]. These comparisons further highlight the promising mechanical performance of the present alloy design, which achieves high stiffness with a considerably lower reinforcement content.

These combined mechanical and thermo-physical results are particularly relevant for structural applications, especially in the aerospace sector, where materials must simultaneously provide high stiffness, strength, low weight, and stable thermomechanical behaviour at elevated temperatures. The demonstrated ability of this alloy system to achieve a high elastic modulus, high strength, and stable high-temperature performance, while preserving good processability in PBF-LB/M, directly addresses key design requirements for weight-critical components. These include the need to minimize structural mass to maximize useable payload, ensure shape and dimensional stability under mechanical loading and thermal cycling, and increase natural frequencies through high specific modulus, thereby reducing resonance risks that may lead to fatigue or catastrophic failure. Moreover, this work suggests a shift in alloy development strategy: instead of adapting existing compositions to AM, the design of new materials should begin with the design of the powder feedstock itself, enabling targeted control over reinforcement distribution, microstructural evolution, and final component performance.

5. Concluding remarks

This work develops a hybrid functionalization method to enhance reinforcement loading in Al2618 composites. The approach combines pre-alloying with Ti and B and high-energy mechanical mixing to decorate the powder surface with discrete TiB_2 particles. This strategy proved effective in producing powder feedstock with a high ceramic fraction, resulting in Al2618 composites with improved processability during PBF-LB/M.

Two different heat treatments, T5 and T6, were studied, revealing distinct microstructural evolution. T5 promotes Al_3Ti and S' precipitates at cell boundaries, while T6 induces Ti–Si-rich needle-like precipitates arranged in a corona-like pattern. These observations suggest a deviation from the typical precipitation and dissolution behaviour of conventional Al2618 alloys.

In terms of mechanical properties, T5 condition exhibited the highest ultimate tensile strength and yield strength. Both T5 and T6 samples showed an elastic modulus higher than that of conventional Al2618 alloy. T6 treatment provided superior thermal properties, with a more stable CTE, due to homogenization and formation of coarse Al_9FeNi phases.

CRediT authorship contribution statement

Giorgia Lupi: Writing – original draft, Methodology, Investigation, Formal analysis, Data curation. **Luca Mariotti:** Writing – review & editing, Methodology, Investigation, Formal analysis, Data curation. **Shenglu Lu:** Writing – review & editing, Investigation, Formal analysis, Data curation. **Wei Xu:** Writing – review & editing, Formal analysis. **Luca Patriarca:** Writing – review & editing, Supervision, Methodology, Investigation, Funding acquisition, Formal analysis, Data curation, Conceptualization. **Riccardo Casati:** Writing – review & editing, Supervision, Resources, Project administration, Methodology, Investigation, Funding acquisition, Formal analysis, Conceptualization.

Declaration of competing interest

The authors declare that they have no known competing financial interests or personal relationships that could have appeared to influence the work reported in this manuscript.

All authors have participated in the preparation of the manuscript and have approved its final version.

Acknowledgements

This study was accomplished within the ENCOMPASS (Design of Enhanced Metal Matrix Composites for Additive Manufacturing of Space Structures) project funded by the European Space Agency. The authors acknowledge the support of the ISIS@MACH ITALIA Research Infrastructure for providing access to the STEM facilities used in this work.

Appendix A. Supplementary data

Supplementary data to this article can be found online at https://doi.org/10.1016/j.msea.2025.149500.

Data availability

Data will be made available on request.

References

[1] T. DebRoy, H.L. Wei, J.S. Zuback, T. Mukherjee, J.W. Elmer, J.O. Milewski, A. M. Beese, A. Wilson-Heid, A. De, W. Zhang, Additive manufacturing of metallic components – process, structure and properties, Undefined 92 (2018) 112–224, https://doi.org/10.1016/J.PMATSCI.2017.10.001.

[2] D. Herzog, V. Seyda, E. Wycisk, C. Emmelmann, Additive manufacturing of metals, Undefined 117 (2016) 371–392, https://doi.org/10.1016/J.ACTAMAT.2016.07.019.

[3] F.I. Azam, A.M. Abdul Rani, K. Altaf, T.V.V.L.N. Rao, H.A. Zaharin, An In-Depth review on direct additive manufacturing of metals, IOP Conf. Ser. Mater. Sci. Eng. 328 (2018) 012005, https://doi.org/10.1088/1757-899X/328/1/012005.

[4] V. Bhavar, P. Kattire, V. Patil, S. Khot, K. Gujar, R. Singh, A review on powder bed fusion technology of metal additive manufacturing, Undefined (2017) 251–253, https://doi.org/10.1201/9781315119106-15.

[5] W.E. King, A.T. Anderson, R.M. Ferencz, N.E. Hodge, C. Kamath, S.A. Khairallah, A.M. Rubenchik, Laser powder bed fusion additive manufacturing of metals; physics, computational, and materials challenges, Undefined 2 (2015) 041304, https://doi.org/10.1063/1.4937809.

[6] P.K. Gokuldoss, S. Kolla, J. Eckert, Additive manufacturing processes: selective laser melting, electron beam melting and binder jetting—selection guidelines, Materials 10 (2017) 672, https://doi.org/10.3390/MA10060672, 672 10 (2017).

[7] A. Mussatto, I.U.I. Ahad, R.T. Mousavian, Y. Delaure, D. Brabazon, Advanced production routes for metal matrix composites, Eng. Rep. 3 (2021) e12330, https://doi.org/10.1002/ENG2.12330.

[8] P.A. Earvolino, M.E. Fine, J.R. Weertman, V.R. Parameswaran, Processing an AlAl3Zr0.25Ti0.75 metal-matrix composite by conventional melting, casting and rolling, Scripta Metall. Mater. 26 (1992) 945–948, https://doi.org/10.1016/0956-716X(92)90687-A.

[9] D. Manfredi, F. Calignano, M. Krishnan, R. Canali, E.P. Ambrosio, S. Biamino, D. Ugues, M. Pavese, P. Fino, Additive manufacturing of Al alloys and aluminium matrix composites (AMCs). https://doi.org/10.5772/58534, 2014.

[10] M.S. Kenevisi, Y. Yu, F. Lin, A review on additive manufacturing of Al–Cu (2xxx) aluminium alloys, processes and defects 37 (2021) 805–829, https://doi.org/10.1080/02670836.2021.1958487. Https://Doi.Org/10.1080/02670836.2021.1958487.

[11] T. Fedina, F. Belelli, G. Lupi, B. Brandau, R. Casati, R. Berneth, F. Brueckner, A.F. H. Kaplan, Influence of AlSi10Mg powder aging on the material degradation and its processing in laser powder bed fusion, Powder Technol. 412 (2022) 118024, https://doi.org/10.1016/J.POWTEC.2022.118024.

[12] C. Pleass, S. Jothi, Influence of powder characteristics and additive manufacturing process parameters on the microstructure and mechanical behaviour of inconel 625 fabricated by selective laser melting, Addit. Manuf. 24 (2018) 419–431, https://doi.org/10.1016/J.ADDMA.2018.09.023.

[13] K. Geng, Y. Yang, S. Li, R.D.K. Misra, Q. Zhu, Enabling high-performance 3D printing of Al powder by decorating with high laser absorbing Co phase, Addit. Manuf. 32 (2020) 101012, https://doi.org/10.1016/J.ADDMA.2019.101012.

[14] T. Romano, A. Ratkus, S. Gruber, M. Pozzi, H. Kos, C. Garion, S. Rorison, E. López, T. Torims, M. Vedani, Pure copper membranes manufactured by green laser powder bed fusion with varying wall-thickness and building orientation: microstructure, properties, and vacuum tightness performance, Vacuum 233 (2025) 113995, https://doi.org/10.1016/J.VACUUM.2024.113995.

[15] F. Belelli, R. Casati, M. Vedani, Development of al-cu-mg and al-mg-si-zr alloys with improved L-PBF processability. https://doi.org/10.1007/978-3-030-92381-5_26, 2022, 289-297.

[16] K. Tian, Y. Zhao, L. Jiao, S. Zhang, Z. Zhang, X. Wu, Effects of in situ generated ZrB2 nano-particles on microstructure and tensile properties of 2024Al matrix composites, J. Alloys Compd. 594 (2014) 1–6, https://doi.org/10.1016/J.JALLCOM.2014.01.117.

[17] X. Nie, H. Zhang, H. Zhu, Z. Hu, L. Ke, X. Zeng, Effect of Zr content on formability, microstructure and mechanical properties of selective laser melted Zr modified Al-4.24Cu-1.97Mg-0.56Mn alloys, J. Alloys Compd. 764 (2018) 977–986, https://doi.org/10.1016/J.JALLCOM.2018.06.032.

[18] K. Jahns, R. Bappert, P. Böhlke, U. Krupp, Additive manufacturing of CuCr1Zr by development of a gas atomization and laser powder bed fusion routine, Int. J. Adv. Manuf. Technol. 107 (2020) 2151–2161, https://doi.org/10.1007/S00170-020-04941-7/FIGURES/12.
[19] X.P. Li, G. Ji, Z. Chen, A. Addad, Y. Wu, H.W. Wang, J. Vleugels, J. Van Humbeeck, J.P. Kruth, Selective laser melting of nano-TiB2 decorated AlSi10Mg alloy with high fracture strength and ductility, Acta Mater. 129 (2017) 183–193, https://doi.org/10.1016/J.ACTAMAT.2017.02.062.
[20] A. Mehta, L. Zhou, T. Huynh, S. Park, H. Hyer, S. Song, Y. Bai, D.D. Imholte, N. E. Woolstenhulme, D.M. Wachs, Y. Sohn, Additive manufacturing and mechanical properties of the dense and crack free Zr-modified aluminum alloy 6061 fabricated by the laser-powder bed fusion, Addit. Manuf. 41 (2021) 101966, https://doi.org/10.1016/j.addma.2021.101966.
[21] Q.Z. Wang, X. Lin, N. Kang, X.L. Wen, Y. Cao, J.L. Lu, D.J. Peng, J. Bai, Y.X. Zhou, M. El Mansori, W.D. Huang, Effect of laser additive manufacturing on the microstructure and mechanical properties of TiB2 reinforced Al-Cu matrix composite, Mater. Sci. Eng., A 840 (2022) 142950, https://doi.org/10.1016/J.MSEA.2022.142950.
[22] Z. Fan, Y. Wang, Y. Zhang, T. Qin, X.R. Zhou, G.E. Thompson, T. Pennycook, T. Hashimoto, Grain refining mechanism in the Al/Al–Ti–B system, Acta Mater. 84 (2015) 292–304, https://doi.org/10.1016/J.ACTAMAT.2014.10.055.
[23] X. Wen, Q. Wang, Q. Mu, N. Kang, S. Sui, H. Yang, X. Lin, W. Huang, Laser solid forming additive manufacturing TiB2 reinforced 2024Al composite: microstructure and mechanical properties, Mater. Sci. Eng., A 745 (2019) 319–325, https://doi.org/10.1016/J.MSEA.2018.12.072.
[24] J. Su, Y. Li, M.G. Duan, S. Liu, K. Liu, Investigation on particle strengthening effect in in-situ TiB2/2024 composite by nanoindentation test, Mater. Sci. Eng., A 727 (2018) 29–37, https://doi.org/10.1016/J.MSEA.2018.04.070.
[25] F. Belelli, R. Casati, F. Larini, M. Riccio, M. Vedani, Investigation on two Ti–B-reinforced Al alloys for laser powder bed fusion, Mater. Sci. Eng., A 808 (2021) 140944, https://doi.org/10.1016/J.MSEA.2021.140944.
[26] F. Belelli, R. Casati, M. Riccio, A. Rizzi, M.Y. Kayacan, M. Vedani, Metals development of a novel high-temperature Al alloy for laser powder bed fusion. https://doi.org/10.3390/met11010035, 2020.
[27] N. Iqbal, N.H. van Dijk, T. Hansen, L. Katgerman, G.J. Kearley, The role of solute titanium and TiB2 particles in the liquid–solid phase transformation of aluminum alloys, Mater. Sci. Eng., A 386 (2004) 20–26, https://doi.org/10.1016/J.MSEA.2004.06.068.
[28] J. Li, F.S. Hage, Q.M. Ramasse, P. Schumacher, The nucleation sequence of α-Al on TiB2 particles in Al-Cu alloys, Acta Mater. 206 (2021) 116652, https://doi.org/10.1016/J.ACTAMAT.2021.116652.
[29] N. Iqbal, N.H. van Dijk, S.E. Offerman, N. Geerlofs, M.P. Moret, L. Katgerman, G. J. Kearley, In situ investigation of the crystallization kinetics and the mechanism of grain refinement in aluminum alloys, Mater. Sci. Eng., A 416 (2006) 18–32, https://doi.org/10.1016/J.MSEA.2005.10.045.
[30] M.X. Zhang, P.M. Kelly, M.A. Easton, J.A. Taylor, Crystallographic study of grain refinement in aluminum alloys using the edge-to-edge matching model, Acta Mater. 53 (2005) 1427–1438, https://doi.org/10.1016/J.ACTAMAT.2004.11.037.
[31] X. Li, G. Li, M.X. Zhang, Q. Zhu, Novel approach to additively manufacture high-strength Al alloys by laser powder bed fusion through addition of hybrid grain refiners, Addit. Manuf. 48 (2021) 102400, https://doi.org/10.1016/J.ADDMA.2021.102400.
[32] A. Durga, N.H. Pettersson, S.B.A. Malladi, Z. Chen, S. Guo, L. Nyborg, G. Lindwall, Grain refinement in additively manufactured ferritic stainless steel by in situ inoculation using pre-alloyed powder, Scr. Mater. 194 (2021) 113690, https://doi.org/10.1016/J.SCRIPTAMAT.2020.113690.
[33] V. Lindström, O. Liashenko, K. Zweiacker, S. Derevianko, V. Morozovych, Y. Lyashenko, C. Leinenbach, Laser powder bed fusion of metal coated copper powders, Materials 13 (2020) 3493, https://doi.org/10.3390/MA13163493. Page 3493 13 (2020).
[34] G. Lupi, M. Poulin, F. Gobber, M. Actis Grande, R. Casati, Improving laser powder bed fusion processability of pure Cu through powder functionalization with Ag, Powder Technol. 444 (2024) 120044, https://doi.org/10.1016/J.POWTEC.2024.120044.
[35] R. Bidulsky, F.S. Gobber, J. Bidulska, M. Ceroni, T. Kvackaj, M.A. Grande, Coated metal powders for laser powder bed fusion (L-PBF) processing: a review, Metals 11 (2021) 1831, https://doi.org/10.3390/met11111831.
[36] Y. Geng, K. Lv, C. Zai, Z. Zhang, A. Kunwar, A high-strength TiB2-Modified al–si–mg–zr alloy fabricated by laser powder-bed fusion, Acta Metall. Sin. 38 (2025) 542–554, https://doi.org/10.1007/S40195-025-01825-1/FIGURES/13.
[37] Y. Meng, Z. Yu, P. Rong, G. Li, Densification behavior, microstructure evolution, and tensile properties of selective laser melting additive manufactured TiB2/AlSi10Mg composite, J. Laser Appl. 32 (2020) 22007, https://doi.org/10.2351/1.5139026/225288.
[38] Y. Li, D. Gu, H. Zhang, L. Xi, Effect of trace addition of ceramic on microstructure development and mechanical properties of selective laser melted AlSi10Mg alloy, Chin. J. Mech. Eng. 33 (2020) 1–13, https://doi.org/10.1186/S10033-020-00448-0/FIGURES/12.
[39] R. Wang, L. Xi, K. Ding, B. Gökce, S. Barcikowski, D. Gu, Powder preparation during ball milling and laser additive manufacturing of aluminum matrix nanocomposites: powder properties, processability and mechanical property, Adv. Powder Technol. 33 (2022) 103687, https://doi.org/10.1016/J.APT.2022.103687.
[40] Q.Z. Wang, X. Lin, N. Kang, X.L. Wen, Y. Cao, J.L. Lu, D.J. Peng, J. Bai, Y.X. Zhou, M. El Mansori, W.D. Huang, Effect of laser additive manufacturing on the microstructure and mechanical properties of TiB2 reinforced Al-Cu matrix composite, Mater. Sci. Eng., A 840 (2022) 142950, https://doi.org/10.1016/J.MSEA.2022.142950.
[41] G. Lupi, L. Mariotti, A. Mistrini, J. Larsson, L. Patriarca, R. Casati, Microstructure and tensile properties of TIB2-reinforced Al-2618 thin walls produced by laser powder bed fusion, Mater. Char. 228 (2025) 115372, https://doi.org/10.1016/j.matchar.2025.115372.
[42] L. Lu, M.O. Lai, H.Y. Wang, Synthesis of titanium diboride TiB2 and Ti-Al-B metal matrix composites, J. Mater. Sci. 35 (2000) 241–248, https://doi.org/10.1023/A:1004789910279/METRICS.
[43] S.Z. Soong, W.L. Lai, A.N. Kay Lup, Atomization of metal and alloy powders: processes, parameters, and properties, AIChE J. 69 (2023) e18217, https://doi.org/10.1002/AIC.18217.
[44] A. Ünal, Production of rapidly solidified aluminium alloy powders by gas atomisation and their applications, Powder Metall. 33 (1990) 53–64, https://doi.org/10.1179/POM.1990.33.1.53.
[45] F. Nový, M. Janeček, R. Král, Microstructure changes in a 2618 aluminium alloy during ageing and creep, J. Alloys Compd. 487 (2009) 146–151, https://doi.org/10.1016/J.JALLCOM.2009.08.014.
[46] Kymera international. https://www.kymerainternational.com/, 2025.
[47] IMR metalle GmbH. https://www.imr-metalle.com/en/products/metal-powders, 2025.
[48] Treibacher industrie AG. https://treibacher.com/en/, 2025.
[49] J.O. Andersson, T. Helander, L. Höglund, P. Shi, B. Sundman, Thermo-calc & DICTRA, computational tools for materials science, Calphad 26 (2002) 273–312, https://doi.org/10.1016/S0364-5916(02)00037-8.
[50] ASTM F3637−23, Standard Guide for Additive Manufacturing of Metal — Finished Part Properties — Methods for Relative Density Measurement, ASTM International, 2023.
[51] R. Casati, J.N. Lemke, A.Z. Alarcon, M. Vedani, Aging behavior of high-strength Al alloy 2618 produced by selective laser melting, Metall Mater Trans A Phys Metall Mater Sci 48 (2017) 575–579, https://doi.org/10.1007/S11661-016-3883-Y/FIGURES/4.
[52] F. Nový, M. Janeček, R. Král, Microstructure changes in a 2618 aluminium alloy during ageing and creep, J. Alloys Compd. 487 (2009) 146–151, https://doi.org/10.1016/J.JALLCOM.2009.08.014.
[53] M. Schuster, A. De Luca, A. Mathur, E. Hosseini, C. Leinenbach, Precipitation in a 2xxx series al-cu-mg-zr alloy fabricated by laser powder bed fusion, Mater. Des. 211 (2021) 110131, https://doi.org/10.1016/J.MATDES.2021.110131.
[54] G. Gyarmati, G. Fegyverneki, Z. Kéri, D. Molnár, M. Tokár, L. Varga, T. Mende, Controlled precipitation of intermetallic (Al,Si)3Ti compound particles on double oxide films in liquid aluminum alloys, Mater. Char. 181 (2021) 111467, https://doi.org/10.1016/J.MATCHAR.2021.111467.
[55] S. Ma, X. Wang, Mechanical properties and fracture of in-situ Al3Ti particulate reinforced A356 composites, Mater. Sci. Eng., A 754 (2019) 46–56, https://doi.org/10.1016/J.MSEA.2019.03.044.
[56] S. Ma, N. Li, C. Zhang, X. Wang, Evolution of intermetallic phases in an al–si–ti alloy during solution treatment, J. Alloys Compd. 831 (2020) 154872, https://doi.org/10.1016/J.JALLCOM.2020.154872.
[57] Y. Wang, Y. Lu, J. Xu, S. Zhang, W. Wu, Z. Chen, The effects of Ti on the precipitation evolution and age-hardening behavior of Al–7Si–Mg alloy, Intermetallics 148 (2022) 107642, https://doi.org/10.1016/J.INTERMET.2022.107642.
[58] F. Bardi, M. Cabibbo, S. Spigarelli, An analysis of thermo-mechanical treatments of a 2618 aluminium alloy: study of optimum conditions for warm forging, Mater. Sci. Eng., A 334 (2002) 87–95, https://doi.org/10.1016/S0921-5093(01)01775-0.
[59] R. Casati, J.N. Lemke, A.Z. Alarcon, M. Vedani, Aging behavior of high-strength Al alloy 2618 produced by selective laser melting, Metall. Mater. Trans. 48 (2017) 575–579, https://doi.org/10.1007/s11661-016-3883-y.
[60] Z. Feng, Y. Yang, B. Huang, M. Han, X. Luo, J. Ru, Precipitation process along dislocations in Al–Cu–Mg alloy during artificial aging, Mater. Sci. Eng., A 528 (2010) 706–714, https://doi.org/10.1016/J.MSEA.2010.09.069.
[61] S.C. Wang, M.J. Starink, Two types of S phase precipitates in Al–Cu–Mg alloys, Acta Mater. 55 (2007) 933–941, https://doi.org/10.1016/J.ACTAMAT.2006.09.015.
[62] S.C. Wang, M.J. Starink, Precipitates and intermetallic phases in precipitation hardening Al-Cu-Mg-(Li) based alloys, Int. Mater. Rev. 50 (2005) 193–215, https://doi.org/10.1179/174328005X14357.
[63] M. Jin, A. Piglione, B. Dovgyy, E. Hosseini, P.A. Hooper, S.R. Holdsworth, M. S. Pham, Cyclic plasticity and fatigue damage of CrMnFeCoNi high entropy alloy fabricated by laser powder-bed fusion, Addit. Manuf. 36 (2020) 101584, https://doi.org/10.1016/J.ADDMA.2020.101584.
[64] T.A. Lebedkina, M.A. Lebyodkin, Effect of deformation geometry on the intermittent plastic flow associated with the Portevin–Le chatelier effect, Acta Mater. 56 (2008) 5567–5574, https://doi.org/10.1016/J.ACTAMAT.2008.07.025.
[65] X. Nie, H. Zhang, H. Zhu, Z. Hu, Y. Qi, X. Zeng, On the role of Zr content into Portevin-Le chatelier (PLC) effect of selective laser melted high strength Al-Cu-Mg-Mn alloy, Mater. Lett. 248 (2019) 5–7, https://doi.org/10.1016/J.MATLET.2019.03.112.
[66] Z. Hu, Y. Qi, X. Nie, H. Zhang, H. Zhu, The Portevin-Le chatelier (PLC) effect in an Al-Cu aluminum alloy fabricated by selective laser melting, Mater. Char. 178 (2021) 111198, https://doi.org/10.1016/J.MATCHAR.2021.111198.
[67] M. Avateffazeli, P.E. Carrion, B. Shachi-Amirkhiz, H. Pirgazi, M. Mohammadi, N. Shamsaei, M. Haghshenas, Correlation between tensile properties,

microstructure, and processing routes of an Al–Cu–Mg–Ag–TiB2 (A205) alloy: additive manufacturing and casting, Mater. Sci. Eng., A 841 (2022) 142989, https://doi.org/10.1016/J.MSEA.2022.142989.
[68] A.A. Shibkov, A.E. Zolotov, M.A. Zheltov, A.A. Denisov, Morphological transition from the euclidean to the fractal shape of the lüders band in the aluminum-magnesium alloy AMg6, Phys. Solid State 53 (2011) 887–895, https://doi.org/10.1134/S1063783411050271.
[69] B.S. Rowlands, C. Rae, E. Galindo-Nava, The Portevin-Le chatelier effect in nickel-base superalloys: origins, consequences and comparison to strain ageing in other alloy systems, Prog. Mater. Sci. 132 (2023) 101038, https://doi.org/10.1016/J.PMATSCI.2022.101038.
[70] R. Schwab, V. Ruff, On the nature of the yield point phenomenon, Acta Mater. 61 (2013) 1798–1808, https://doi.org/10.1016/J.ACTAMAT.2012.12.003.
[71] M. Safi, M.K. Hassanzadeh-Aghdam, M.J. Mahmoodi, Effects of nano-sized ceramic particles on the coefficients of thermal expansion of short SiC fiber-aluminum hybrid composites, J. Alloys Compd. 803 (2019) 554–564, https://doi.org/10.1016/J.JALLCOM.2019.06.314.
[72] L.D. Wang, W.D. Fei, L.S. Jiang, C.K. Yao, New aluminum matrix composite with much lower coefficient of thermal expansion and higher strength, J. Mater. Sci. Lett. 21 (2002) 737–738, https://doi.org/10.1023/A:1015749408728/METRICS.
[73] T. Hanemann, L.N. Carter, M. Habschied, N.J.E. Adkins, M.M. Attallah, M. Heilmaier, In-situ alloying of AlSi10Mg+Si using selective laser melting to control the coefficient of thermal expansion, J. Alloys Compd. 795 (2019) 8–18, https://doi.org/10.1016/J.JALLCOM.2019.04.260.
[74] N.J. Harrison, I. Todd, K. Mumtaz, Thermal expansion coefficients in invar processed by selective laser melting, J. Mater. Sci. 52 (2017) 10517–10525, https://doi.org/10.1007/S10853-017-1169-4/TABLES/3.
[75] X.L. Wang, C.M. Hoffmann, C.H. Hsueh, G. Sarma, C.R. Hubbard, J.R. Keiser, Influence of residual stress on thermal expansion behavior, Appl. Phys. Lett. 75 (1999) 3294–3296, https://doi.org/10.1063/1.125329.
[76] N.M. Siddesh Kumar, Dhruthi, G.K. Pramod, P. Samrat, M. Sadashiva, A critical review on heat treatment of aluminium alloys, Mater. Today Proc. 58 (2022) 71–79, https://doi.org/10.1016/J.MATPR.2021.12.586.
[77] X.Y. Wang, J. Yang, P.Z. Chi, E. Bahonar, M. Tayebi, Effects of the microstructure and precipitation hardening on the thermal expansion behavior of ZK60 magnesium alloy, J. Alloys Compd. 901 (2022) 163422, https://doi.org/10.1016/J.JALLCOM.2021.163422.
[78] R. Gupta, G.P. Chaudhari, B.S.S. Daniel, Effect of in-situ formed Al3Ti particles on the microstructure and mechanical properties of 6061 Al alloy, IOP Conf. Ser. Mater. Sci. Eng. 330 (2018) 012012, https://doi.org/10.1088/1757-899X/330/1/012012.
[79] X. Zhu, R. Wang, C. Peng, W. Liu, J. Peng, Microstructure and thermal expansion behavior of spray-formed Al–27Si alloy used for electronic packaging, J. Mater. Sci. Mater. Electron. 25 (2014) 4889–4895, https://doi.org/10.1007/S10854-014-2249-8/TABLES/1.
[80] X.C. Tong, High thermal conductivity metal matrix composites, Springer Series in Advanced Microelectronics 30 (2011) 233–276, https://doi.org/10.1007/978-1-4419-7759-5_6.
[81] D. Duschlbauer, H.J. Böhm, H.E. Pettermann, Numerical simulation of thermal conductivity of MMCs: effect of thermal interface resistance. https://doi.org/10.1179/026708303225004305, 2003, 19, 1107-1114.
[82] A. Miranda, N. Barekar, B.J. McKay, MWCNTs and their use in Al-MMCs for ultra-high thermal conductivity applications: a review, J. Alloys Compd. 774 (2019) 820–840, https://doi.org/10.1016/J.JALLCOM.2018.09.202.
[83] A. Suzuki, S. Miyake, W. Naruse, N. Takata, M. Kobashi, Synthesis of porous Al/Al3Ti composite with hierarchical open–cell structure for combining with phase change material, J. Alloys Compd. 770 (2019) 1100–1111, https://doi.org/10.1016/J.JALLCOM.2018.08.211.
[84] S.H. Kayani, S.U. Lee, K. Euh, J.M. Lee, Y.H. Cho, Effect of as-cast microstructure on precipitation behavior and thermal conductivity of T5-treated Al7Si0.35Mg alloy, J. Alloys Compd. 976 (2024) 173004, https://doi.org/10.1016/J.JALLCOM.2023.173004.
[85] A. Ghasemi, E. Fereiduni, M. Balbaa, M. Elbestawi, S. Habibi, Unraveling the low thermal conductivity of the LPBF fabricated pure Al, AlSi12, and AlSi10Mg alloys through substrate preheating, Addit. Manuf. 59 (2022) 103148, https://doi.org/10.1016/J.ADDMA.2022.103148.
[86] S.W. Choi, H.S. Cho, S. Kumai, Effect of the precipitation of secondary phases on the thermal diffusivity and thermal conductivity of Al-4.5Cu alloy, J. Alloys Compd. 688 (2016) 897–902, https://doi.org/10.1016/J.JALLCOM.2016.07.137.
[87] H. Zhang, H. Zhu, X. Nie, J. Yin, Z. Hu, X. Zeng, Effect of zirconium addition on crack, microstructure and mechanical behavior of selective laser melted Al-Cu-Mg alloy, Scr. Mater. 134 (2017) 6–10, https://doi.org/10.1016/J.SCRIPTAMAT.2017.02.036.
[88] Z.W. Du, G.J. Wang, X.L. Han, Z.H. Li, B.H. Zhu, X. Fu, Y.A. Zhang, B.Q. Xiong, Microstructural evolution after creep in aluminum alloy 2618, J. Mater. Sci. 47 (2012) 2541–2547, https://doi.org/10.1007/S10853-011-6077-4/FIGURES/10.
[89] X. Chen, C.D. Marioara, S.J. Andersen, J. Friis, A. Lervik, R. Holmestad, E. Kobayashi, Precipitation processes and structural evolutions of various GPB zones and two types of S phases in a cold-rolled Al-Mg-Cu alloy, Mater. Des. 199 (2021) 109425, https://doi.org/10.1016/J.MATDES.2020.109425.
[90] S.P. Ringer, K. Hono, I.J. Polmear, T. Sakurai, Precipitation processes during the early stages of ageing in Al□Cu□Mg alloys, Appl. Surf. Sci. 94–95 (1996) 253–260, https://doi.org/10.1016/0169-4332(95)00383-5.
[91] H. Lu, P. Kadolkar, K. Nakazawa, T. Ando, C.A. Blue, Precipitation behavior of AA2618, Metall. Mater. Trans. 38 (2007) 2379–2388, https://doi.org/10.1007/s11661-007-9295-2.
[92] M. Kun, L. Tingting, L. Ya, S. Xuping, W. Jianhua, Study on strengthening and toughening mechanisms of aluminum alloy 2618-Ti at elevated temperature, High Temp. Mater. Process. 37 (2018) 9–15, https://doi.org/10.1515/HTMP-2015-0226/MACHINEREADABLECITATION/RIS.
[93] R. Casati, J. Fiocchi, A. Fabrizi, N. Lecis, F. Bonollo, M. Vedani, Effect of ball milling on the ageing response of Al2618 composites reinforced with SiC and oxide nanoparticles, J. Alloys Compd. 693 (2017) 909–920, https://doi.org/10.1016/J.JALLCOM.2016.09.265.
[94] K. Hu, C. Zou, H. Wang, Z. Wei, The role of in-situ Al3Ti formed during solidification in improving the high-temperature properties of Al–Cu alloy, Mater. Sci. Eng., A 902 (2024) 146585, https://doi.org/10.1016/J.MSEA.2024.146585.
[95] E. Basiri Tochaee, H.R. Madaah Hosseini, S.M. Seyed Reihani, Fabrication of high strength in-situ Al-Al3Ti nanocomposite by mechanical alloying and hot extrusion: investigation of fracture toughness, Mater. Sci. Eng., A 658 (2016) 246–254, https://doi.org/10.1016/J.MSEA.2016.02.010.
[96] L. Xi, L. Feng, D. Gu, K.G. Prashanth, I. Kaban, R. Wang, K. Xiong, B. Sarac, J. Eckert, Microstructure formation and mechanical performance of micro-nanoscale ceramic reinforced aluminum matrix composites manufactured by laser powder bed fusion, J. Alloys Compd. 939 (2023) 168803, https://doi.org/10.1016/J.JALLCOM.2023.168803.
[97] J.M. Kunze, C.C. Bampton, Challenges to developing and producing MMCs for space applications, Undefined 53 (2001) 22–25, https://doi.org/10.1007/S11837-001-0141-5.
[98] A.S.M. International, Volume 4 - heat treating, in: ASM Metals Handbook, 1991 n. d.
[99] M. Kun, L. Tingting, L. Ya, S. Xuping, W. Jianhua, Study on strengthening and toughening mechanisms of aluminum alloy 2618-Ti at elevated temperature, High Temp. Mater. Process. 37 (2018) 9–15, https://doi.org/10.1515/htmp-2015-0226.
[100] S. Ma, Y. Wang, X. Wang, Microstructures and mechanical properties of an Al-Cu-Mg-Sc alloy reinforced with in-situ TiB2 particulates, Mater. Sci. Eng., A 788 (2020) 139603, https://doi.org/10.1016/J.MSEA.2020.139603.
[101] M.H. Ghoncheh, M. Sanjari, A.S. Zoeram, E. Cyr, B.S. Amirkhiz, A. Lloyd, M. Haghshenas, M. Mohammadi, On the microstructure and solidification behavior of new generation additively manufactured Al-Cu-Mg-Ag-Ti-B alloys, Addit. Manuf. 37 (2021) 101724, https://doi.org/10.1016/J.ADDMA.2020.101724.
[102] A. Aversa, G. Marchese, M. Lorusso, F. Calignano, S. Biamino, E.P. Ambrosio, D. Manfredi, P. Fino, M. Lombardi, M. Pavese, Microstructural and mechanical characterization of aluminum matrix composites produced by laser powder bed fusion. https://doi.org/10.1002/adem.201700180, 2017.
[103] T. Sun, J. Chen, Y. Wu, M. Wang, Y. Fu, H. Wang, H. Wang, Achieving excellent strength of the LPBF additively manufactured Al–Cu–Mg composite via in-situ mixing TiB2 and solution treatment, Mater. Sci. Eng., A 850 (2022) 143531, https://doi.org/10.1016/j.msea.2022.143531.
[104] Q.Z. Wang, X. Lin, N. Kang, X.L. Wen, Y. Cao, J.L. Lu, D.J. Peng, J. Bai, Y.X. Zhou, M. El Mansori, W.D. Huang, Effect of laser additive manufacturing on the microstructure and mechanical properties of TiB2 reinforced Al-Cu matrix composite, Mater. Sci. Eng., A 840 (2022) 142950, https://doi.org/10.1016/j.msea.2022.142950.
[105] M. Schuster, A. De Luca, D. Kucajda, E. Hosseini, R. Widmer, X. Maeder, C. Leinenbach, Heat treatment response and mechanical properties of a Zr-modified AA2618 aluminum alloy fabricated by laser powder bed fusion, J. Alloys Compd. 962 (2023) 171166, https://doi.org/10.1016/J.JALLCOM.2023.171166.
[106] S. Ma, M. Wang, Y. Wu, Y. Li, J. Liu, H. Wang, Z. Chen, Laser powder bed fusion of an ultrafine microstructural in-situ TiB2/Al composite with excellent mechanical properties and thermal stability at elevated temperatures, Mater. Sci. Eng., A 891 (2024) 145969, https://doi.org/10.1016/J.MSEA.2023.145969.
[107] S. Ma, Z. Shang, A. Shang, P. Zhang, C. Tang, Y. Huang, C.L.A. Leung, P.D. Lee, X. Zhang, X. Wang, Additive manufacturing enabled synergetic strengthening of bimodal reinforcing particles for aluminum matrix composites, Addit. Manuf. 70 (2023) 103543, https://doi.org/10.1016/J.ADDMA.2023.103543.